Icing Condition Assessment of In-Service Glass Insulators Based on Graphical Shed Spacing and Graphical Shed Overhang

Yanpeng Hao [1], Jie Wei [1], Xiaolan Jiang [1], Lin Yang [1,*], Licheng Li [1], Junke Wang [2], Hao Li [2] and Ruihai Li [2]

[1] School of Electric Power, South China University of Technology, Guangzhou 510640, China;
yphao@scut.edu.cn (Y.H.); epjie1123@scut.edu.cn (J.W.); jane-jiang@foxmail.com (X.J.); lilc@scut.edu.cn (L.L.)

[2] Electric Power Research Institute, China Southern Power Grid, Guangzhou 510080, China;
wangjk@csg.cn (J.W.); lihao@csg.cn (H.L.); lirh@csg.cn (R.L.)

[*] Correspondence: eplyang@scut.edu.cn; Tel.: +86-159-8918-4979

Abstract: Icing on transmission lines might lead to ice flashovers of insulators, collapse of towers, tripping faults of transmission lines, and other accidents. Shed spacing and shed overhang of insulators are clues for evaluating the probability of ice flashover. This paper researches image-processing methods for the natural icing of in-service glass insulators. Calculation methods of graphical shed spacing and graphical shed overhang are proposed via recognizing the convexity defects of the contours of an icing insulator string based on the GrabCut segmentation algorithm. The experiments are carried out with image data from our climatic chamber and the China Southern Power Grid Disaster (Icing) Warning System of Transmission Lines. The results show that the graphical shed overhang of insulators show evident change due to icing. This method can recognize the most serious icing conditions where the insulator sheds are completely bridged. Also, it can detect bridging positions including the left side, right side, or both sides of the insulator strings in the images.

Keywords: in-service glass insulator; icing condition; image processing; convexity defect; graphical shed spacing; graphical shed overhang

1. Introduction

Icing on transmission lines might lead to ice flashovers of insulators, collapse of towers, tripping faults of transmission lines, and other accidents [1]. The main reasons for ice flashover include: the electrolyte of pollution from air and insulator surface increasing freezing-water capacity; the ice bridging between two adjacent insulators sheds leading to decline of icing flashover voltage [2–4].

Insulator surface pollution is the main reason for flashover occuring in distribution lines. It can also be affected by multiple factors including temperature, humidity, wind velocity, rain and fog, property and quantity of pollution sources, insulator configuration (represented by equivalent salt deposit density (ESDD)), leakage current, and surface pollution layer capacity (SPLC) [5–7]. In recent years, there have been many methods to assess the contamination of insulators based on artificial neural networks (ANN) [5], multi model partitioning filter (MMPF) [6], etc. Also, insulator icing flashover is affected by meteorological conditions, including ice type and structure [7]. However, there are no appropriate methods to denote and assess icing conditions between insulator sheds.

With the development of computer graphics, scholars have started to research insulator condition monitoring based on video or image processing [7,8]. Image processing of icing transmission lines has been researched widely due to its regular configuration. Chongqing University analyzed transmission

line and insulator surface icing images based on edge extraction methods [9]. Xi'an Polytechnic University applied image matching to transmission line galloping monitoring using image gray processing, image enhancement method, and image segmentation [10]. Some scholars have researched equivalent icing thickness representation for transmission lines based on LOG operator edge detection, wavelet multi-scale analysis, and Hough conversion [11–13].

The graphical processing method of icing insulators has recently gained attention. Dalian Maritime University proposed a segmentation method of aerial insulator based on principal component analysis and an active contour model [14,15]. The Chinese Academy of Sciences detected insulators in video sequences using tilt correction, feature extraction, and a support vector machine (SVM) [16]. North China Electric Power University extracted insulator margins from aerial photos using a non-subsampled contourlet transform (NSCT) [17].

Ice morph is complex and fickle [18], which adds difficulty in research to recognize icing degree by image processing. Xi'an Polytechnic University proposed to segment insulators from images before and after icing, and estimate icing degree by comparing insulator contour before and after icing. Nevertheless, this was not verified by experiment [19]. Chongqing University proposed a method to monitor insulator's icing by calculating the volume difference before and after icing based on three-dimensional reconstruction and then calculating ice mass according to rime density (0.5 g/cm^3) [20,21]. However, it is hard to install cameras and power on-site; three-dimensional reconstruction needs at least three cameras. The method used for calculating icing thickness on transmission lines was not applicable for insulators due to their complex structure.

In this paper, the GrabCut segmentation algorithm is proposed to segment ice-covered insulators from images. Compared with the other four image processing methods, the results of GrabCut are superior in terms of contour smoothness and accuracy. For analyzing insulator icing conditions quantitatively, we define and make use of two effective parameters (i.e., graphical shed overhang and graphical shed spacing) to recognize convexity defect of ice-covered insulator string contour. The axial and the radial icing bridge degrees between insulator sheds are denoted by the change of graphical shed spacing and graphical shed overhang. Using image data from our climatic chamber and the China Southern Power Grid Disaster (Icing) Warning System of Transmission Lines, graphical shed spacing and graphical shed overhang are comparatively investigated as a new evaluation method for glass insulator icing conditions.

2. Theory and Method

As the contours of insulator string are convex graphical shed spacing (D) and graphical shed overhang (P) are calculated by recognizing convexity defect of insulator contours after GrabCut-based segmentation.

2.1. Image Segmentation by GrabCut

2.1.1. Maximum Flow and Minimum Cut

The key of GrabCut image segmentation is to determine the graphical maximum flow and minimum cut under maximum flow.

Firstly, an image is mapped to a capacity network where each graphical pixel corresponds to a node. In addition, there are two extra nodes, a source node (s) and a sink node (t). s represents the foreground (or research object) and t represents background (i.e., the image except for the research object), as shown in Figure 1.
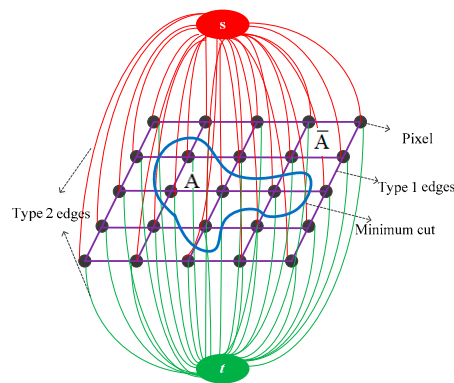
Figure 1. Schematic diagram of GrabCut segmentation.

There are two types of edges: (1) the edges that link adjacent pixels and (2) the edges that link pixels to s or t. $U_{m,n}$, the capacity of type 1 edges, represents the capacity between adjacent pixels m and n; $U_{n,s}$ and $U_{n,t}$, the capacity of type 2 edges, respectively represent the capacity between pixel n and s or n and t. The capacity of type 1 edges denotes a difference between adjacent pixels, and the capacity of type 2 edges denotes the probability that a pixel belongs to the foreground or background. For example, if a pixel belongs to foreground, the capacity (the probability that it belongs to foreground) between the pixel and s is the maximum value, and the capacity (the probability that it belongs to background) between the pixel and t is 0. If the pixel belongs to background for certain, the capacity between the pixel and s is 0, and the capacity between the pixel and t is the maximum value. If a pixel does not belong to the foreground or the background, the capacity between the pixel and s or t is between 0 and the maximum value. The calculations of $U_{m,n}$, $U_{n,s}$, and $U_{n,t}$ are detailed in Section 2.1.2.

If P is the full set, to a set A, existing $m \in A \subset P$, $n \in P - A = \overline{A}$, then $(A, \overline{A})$ is a cut set or "cut" of the network, and $c(A) = \sum\limits_{m \in A, n \subset \overline{A}} U_{m,n}$ is the cut magnitude. An A directed flow network is shown in Figure 2, where the flow of edges describes the amount of capacity that is in use. In Figure 2, the first number on each edge represents the capacity and the second represents the current flow. If $A = \{e, a, b\}$, $\overline{A} = \{c, d, f\}$, and $(A, \overline{A}) = \{(e, d), (a, d), (b, d), (b, f)\}$ is a cut of the network, and the cut magnitude = 7 + 5 + 2 + 5 = 19.
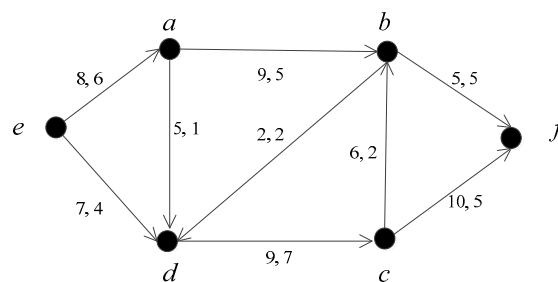

Figure 2. Flow network diagram.

In any network, the maximum flow corresponds to the cut magnitude under the minimum cut. In Figure 1, the minimum cut corresponds to the maximum flow from s, through pixels, to t. The deduction and calculation for maximum flow and minimum cuts in maximum flow is detailed in literature [22].

If the minimum cut of $(A, \overline{A})$ is shown as the blue closed curve in Figure 2 using maximum flow algorithm, A consists of all nodes in the blue closed curve and the source s, while $\overline{A}$ consists of all nodes that are beyond the blue closed curve and the sink t. The pixel points could be segmented to the foreground or background according to the minimum cut.

2.1.2. Calculation Method of $U_{m,n}$, $U_{n,s}$, and $U_{n,t}$

The formula to calculate $U_{m,n}$, the capacity of type 1 edges, is shown in Equation (1) [22]

$$U_{m,n} = \gamma \sum_{(m,n) \in C} e^{-\beta \|z_n - z_m\|^2} \tag{1}$$

where z_m and z_n, respectively, denote color grey level of pixel m and n, β denotes the priority of type 1 edges over type 2 edges, C represents a pair of neighboring pixels, and the exponential coefficient is used to adapt the contrast degree of the image. β can magnify this difference when the contrast degree of the image is low, which is shown in

$$\beta = \left(\frac{2}{N} \left\langle \sum_{(m,n) \in C} (z_m - z_n)^2 \right\rangle \right)^{-1} \tag{2}$$

where $\sum_{(m,n) \in C} (z_m - z_n)^2$ denotes the sum of all neighboring pixel pairs in the image, and N denotes the number of m and n pairs.

The calculation of $U_{n,s}$ and $U_{n,t}$ (i.e., the capacity of type 2 edges) is described as follows.

If n is determined as part of the foreground, $U_{n,s}$ is assigned as L (take $L = 9\gamma$, with the definition of γ identical to that in Equation (1)) and $U_{n,t}$ as 0. If n is determined as part of the background, $U_{n,s}$ is assigned as 0 and $U_{n,t}$ as L.

Otherwise, if n cannot be determined as part of the background or foreground, $U_{n,s}$ and $U_{n,t}$ is determined by a Gaussian mixture model. Assume that the Gaussian mixture model is shown through Equations (3) and (4).

$$G_a = \sum_{i=1}^{K} w_{a,i} g_{a,i}(z_n; \mu_{a,i}, \sigma_{a,i}) \tag{3}$$

$$g(z_n; \mu_{a,i}, \sigma_{a,i}) = \frac{1}{\sqrt{(2\pi)^d |\sigma_{a,i}|}} \exp\left(-\frac{1}{2} (z_n - \mu_{a,i})^T \sigma_{a,i}^{-1} (z_n - \mu_{a,i}) \right) \tag{4}$$

where $\sum_{i=1}^{K} w_{a,i} = 1$ and $0 \leq w \leq 1$, K is the element number of the Gaussian mixture model, which is 3 in this paper. a can be s or t, if a is assigned as s, G_s represents the Gaussian mixture model of the foreground; if a is assigned as t, G_t represents the Gaussian mixture model of the background; $w_{a,j}$ represents the weights of the ith Gaussian model $g(z_n; \mu_{a,I}, \sigma_{a,i})$; z_n represents the pixel to be segmented, where $\mu_{a,i}$ and $\sigma_{a,i}$, respectively, represent the mean value and covariance matrix of the ith Gaussian model.

The calculation of $U_{n,s}$ and $U_{n,t}$ are respectively shown as Equations (5) and (6) [23]

$$U_{n,s} = -\log(G_s) = -\log w_{s,i} + \frac{1}{2} \log |s_{s,i}| + \frac{1}{2} (z_n - \mu_{s,i})^T \sigma_{s,i}^{-1} (z_n - \sigma_{s,i}) \tag{5}$$

$$U_{n,t} = -\log(G_t) = -\log w_{t,i} + \frac{1}{2} \log |s_{t,i}| + \frac{1}{2} (z_n - \mu_{t,i})^T \sigma_{t,i}^{-1} (z_n - \sigma_{t,i}) \tag{6}$$

2.1.3. GrabCut Segmentation Algorithm

This paper analyzes the images of transmission line glass insulators using the GrabCut segmentation algorithm, whose flowchart is shown as Figure 3.

First, G_s or G_t is initialized according to selected rectangle in images; the pixels inside the rectangle are for G_s, and pixels outside the rectangle are for G_t. Next, pixels for G_s and G_t are divided into K classes respectively using a clustering algorithm based on the color grey value. The G_s or G_t belongs to the ith Gaussian model. This paper uses a K-means [23] clustering algorithm, and K is equal to 3.

Next, the parameters for mean value ($\mu_{a,i}$) and covariance matrix ($\sigma_{a,i}$) are calculated for each element in Gaussian mixture model according to color grey value of pixels in each class.

Then, the parameters z_m, z_n, $\mu_{a,i}$, and $\sigma_{a,i}$ are put into Equations (1), (5), and (6). The capacities of the two edge types (i.e., $U_{m,n}$, $U_{n,s}$, and $U_{n,t}$) are calculated. Finally, the object is segmented using the maximum flow algorithm described in Section 2.1.1.

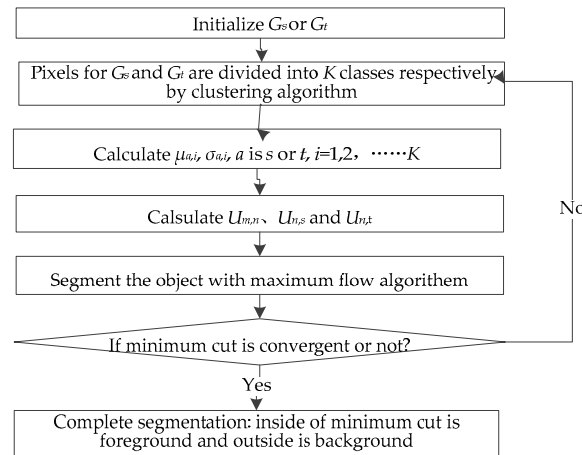This is repeated from the clustering algorithm until the minimum cut is convergent.

Figure 3. Flow chart of GrabCut algorithm for segmentation of ice-covered in-service glass insulators.

2.2. Convex Hull and Convexity Defect

The contour of the insulator string from images before icing could be seen as a concave polygon, and its concavity would decrease with ice accretion. The contour may even become a convex polygon with severe ice accretion. Therefore, the contour of the insulator string from images may reflect the icing situation of insulators.

The convex hull of a concave polygon refers to its minimum enclosing convex polygon, and the convexity defect of a concave polygon refers to the complementary part for the concave polygon to be convex [24]. For example, the contour, convex hull, and convexity defect of two adjacent glass insulator sheds in Figure 4a are shown as Figure 4b, the black line indicates contour, the green line indicates the convex hull and the purple region indicates the convexity defect.
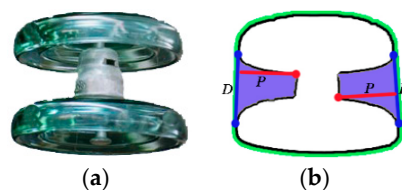

Figure 4. Convex hull and convexity defect of two adjacent glass insulator sheds. (**a**) the original image, (**b**) the processed image.

There are three important parameters for a convexity defect: starting point, ending point, and depth. As shown in Figure 4b, the starting point and ending point are intersection points of convex hull and convexity defect, which are marked with blue points. The deepest point of a convexity defect is one with maximum vertical distance from contours of insulator to convex hull, which is marked with a red point. The depth of a convexity defect refers to the vertical distance from the deepest point to the line D determined by the starting and ending points.

2.3. Computation of Graphical Shed Spacing and Graphical Shed Overhang

The computation flow chart is shown as Figure 5. First, the convex hull and convexity defect are calculated. The images of ice-covered and non-ice-covered insulator string are segmented using the GrabCut algorithm, which can take two insulators' contours. The insulators' contours are presented as many concaves, and convex hull are consist of pixels belonging to minimum convex set on the contours [24]. The starting point, ending point, and depth are calculated.
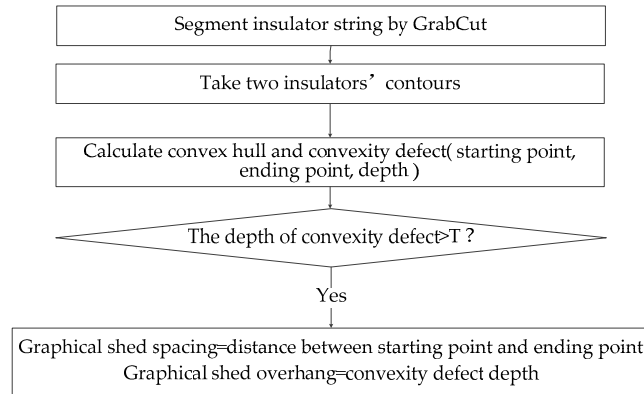

Figure 5. Computation of graphical shed spacing and graphical shed overhang.

Then, there may be many small concaves on insulator contours, especially in icing conditions because ice forms are irregular. However, only the changes in the concaves between adjacent sheds are a cause for concern. This paper selects convexity defects with depth less than *T*. The value of *T* depends on the size of an insulator shed in pixel, which is set to 10 in this paper.

According to the starting point, ending point, and depth, the graphical shed spacing is approximately equal to the distance between the starting point and ending point (*D*), and the graphical shed overhang is approximately equal to the convexity defect depth (*P*). The computation results are represented as a distance measured pixels distance.

2.4. Relationship of Graphical Shed Spacing, Graphical Shed Overhang, and Icing Degree

The insulators before and after icing are shown in orthographic in Figure 6. In Figure 6b, both the upper and lower surface of insulator sheds are covered with ice and the shed spacing are bridged by icicles. It is deduced that the change of *D* and *P* may relate to icing degree.
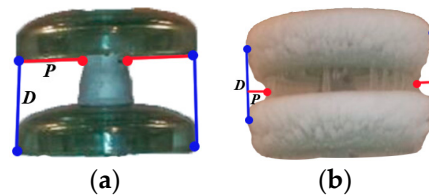

Figure 6. The change of graphical shed spacing (*D*) and graphical shed overhang (*P*), (**a**) before icing, (**b**) after icing.

The bridging degree may differ for insulator sheds from the same insulator string. We can estimate icing degree of the whole insulator string according to the average change percent of *D* and *P*, represented as $\triangle D_a$ (%) and $\triangle P_a$ (%), respectively, and shown in Equations (7) and (8) below.

$$\Delta D_a\,(\%)\;=\;\frac{\sum_{i=1}^{N-1}[(D_{il}{\prime}+D_{ir}{\prime})-(D_{il}+D_{ir})]}{\sum_{i=1}^{n-1}(D_{il}\,+\,D_{ir})} \tag{7}$$

$$\Delta P_a\,(\%) \;=\; \frac{\sum_{i=1}^{N-1}\left[(P_{il}{}' + P_{ir}{}') - (P_{il} + P_{ir})\right]}{\sum_{i=1}^{n-1}(P_{il} \,+\, P_{ir})} \tag{8}$$

where N denotes the number of insulator sheds. D_{il} and D_{ir} denote respectively the left and the right graphical shed spacing between the ith and the number $(i + 1)$th sheds. P_{il} and P_{ir} respectively denote the left and the right graphical shed overhang between the ith and the number $(i + 1)$th sheds. $D_{il}{}'$, $D_{ir}{}'$, $P_{il}{}'$, and $P_{ir}{}'$ denote the related graphical shed spacing and shed overhang after icing.

3. Results and Discussion

In this section, the segmentation results of GrabCut are presented and compared the performance with threshold method [25], Sobel method, Canny method [26], and seed region growth method [27]. Then, to make quantitative analysis of icing conditions, the change of graphical shed overhang and graphical shed spacing are discussed in different icing conditios.

3.1. Image Processing Results and Comparisons

Figure 7 shows the segmentation results in terms of five image processing methods. It is clearly shown that the contours of ice-covered insulator are not segmented properly from background by Threshold method. Figure 7c,d are the results of Sobel and Canny method based on edge detection algorithm, although better segmentations are obtained, there are still a lot of edges from the background that is not enough to accurately monitor icing conditions. Figure 7e shows the segmentation results using seed region growth method. However, the contours of ice-covered insulator are irregular and the threshold values have to be set based on various icing conditions [27]. As shown in Figure 7f, the segmentation results of GrabCut are superior to the other four methods in terms of the contour smoothness and accuracy.
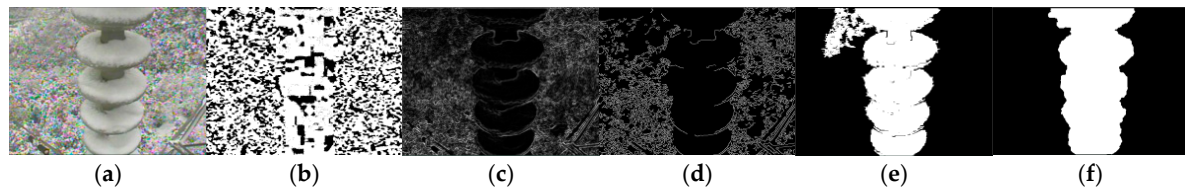

(a)   **(b)**   **(c)**   **(d)**   **(e)**   **(f)**

Figure 7. Experiments of six image segmentation methods for ice-covered insulator, (**a**) original images, (**b**) threshold method, (**c**) Sobel, (**d**) Canny, (**e**) seed region growth method, (**f**) GrabCut.

Based on observing that the contours could be segmented as an enclosing convex polygon using GrabCut, two parameters (i.e., graphical shed overhang and graphical shed spacing) are defined and leveraged using the contour convexity defect recognition. In contrast, the other four methods cannot get graphical shed spacing and graphical shed overhang to analyze icing conditions quantitatively.

To demonstrate the effectiveness of the method we proposed, the experiments are carried out with image data from our climatic chamber and China Southern Power Grid Disaster (Icing) Warning System of Transmission Lines. By the above analysis, insulator icing conditions of four groups are estimated based on the changes of graphical shed spacing and graphical shed overhang. Group 1 is from our climatic chamber with a humidity of 100% and a water conductivity of 2.5×10^{-2} S/m, and the other three groups (i.e., Group 2, Group 3, and Group 4) are from China Southern Power Grid Disaster (Icing) Warning System of Transmission Lines. The sizes of these images from these two sources are 375×256 and 640×480, respectively.

The four groups of insulator images include images without ice and that with ice. Their segmentation results using GrabCut are shown in Figure 8. There convex hull and convexity defect are shown in Figures 9–12.
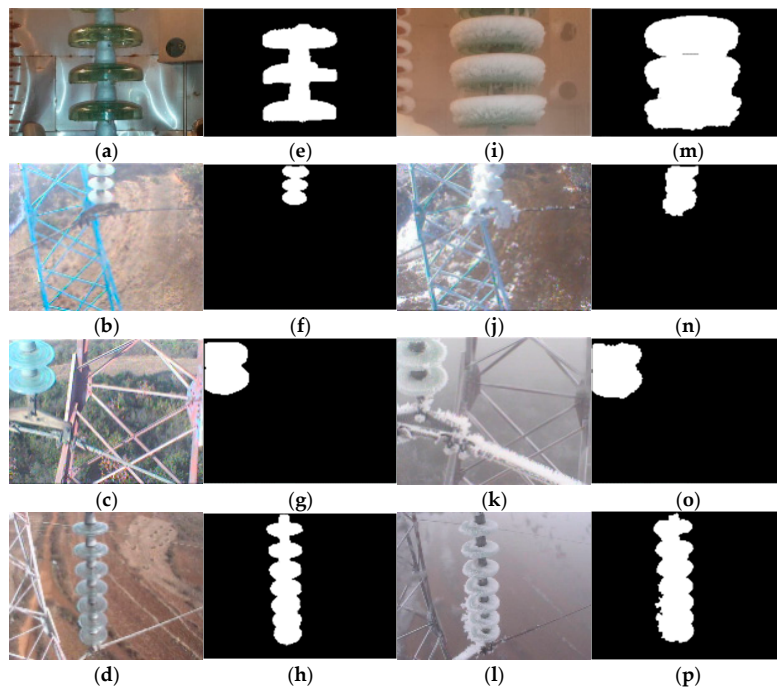
Figure 8. Insulators without ice (**a**–**d**) and their GrabCut segmentation results (**e**–**h**), and insulators with ice (**i**–**l**) and their GrabCut segmentation results (**m**–**p**).

Figure 9. Insulators without ice (**a**,**b**) and their convexity hulls and defects of adjacent sheds (**c**,**d**), and insulators with ice (**e**,**f**) and their convexity hulls and defects of adjacent sheds (**g**,**h**) in Group 1.

Figure 10. Insulators without ice (**a**,**b**) and their convexity hulls and defects of adjacent sheds (**c**,**d**), and insulators with ice (**e**,**f**) and their convexity hulls and defects of adjacent sheds (**g**,**h**) in Group 2.
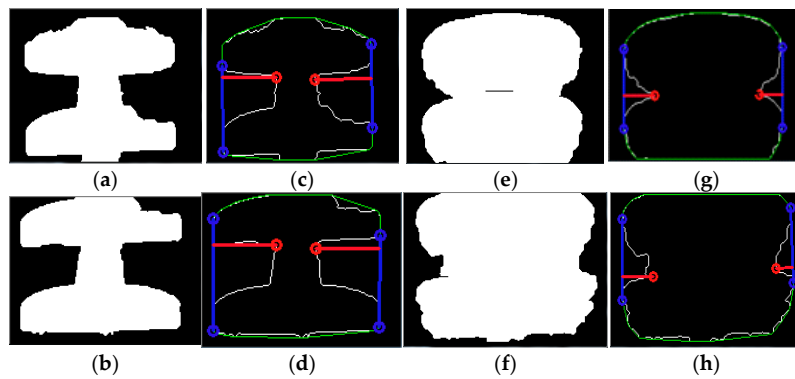
Figure 11. Insulators without ice (**a**) and their convexity hulls and defects of adjacent sheds (**c**), and insulators with ice (**b**) and their convexity hulls and defects of adjacent sheds (**d**) in Group 3.
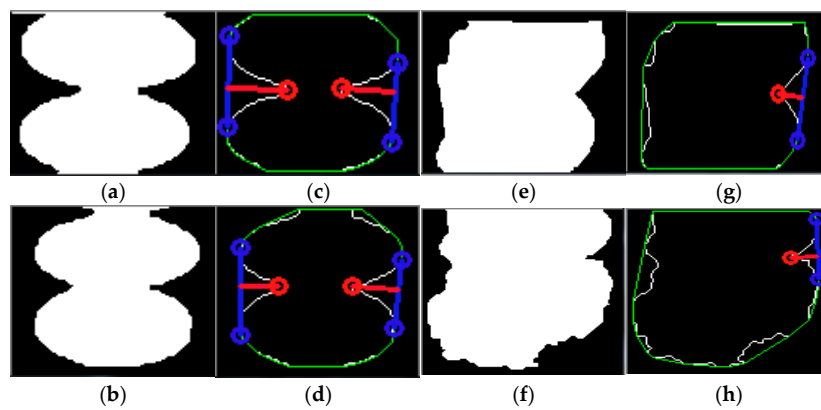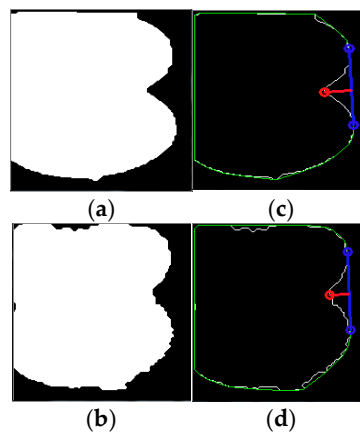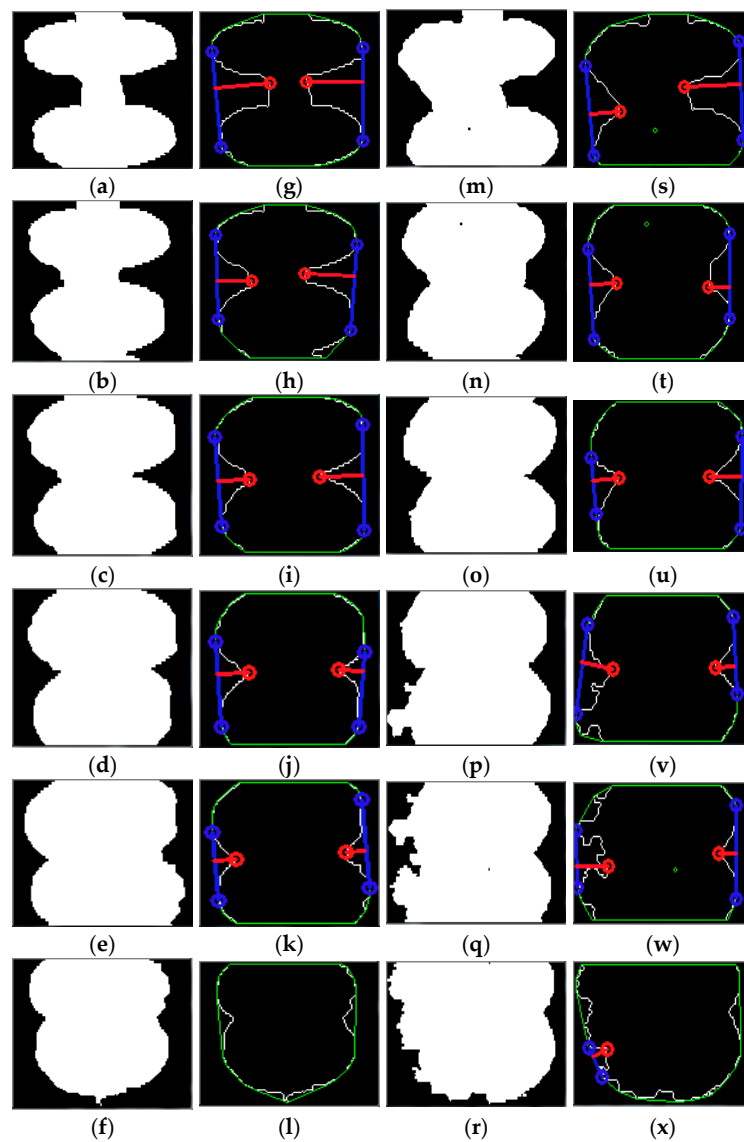

Figure 12. Insulators without ice (**a**–**f**) and their convexity hulls and defects of adjacent sheds (**g**–**l**), and insulators with ice (**m**–**r**) and their convexity hulls and defects of adjacent sheds (**s**–**x**) in Group 4.

3.2. The Change of Graphical Shed Overhang and Spacing in Different Icing Conditions

Based on the results of insulator convexity defect from Figures 9–12, we get percentage changes of insulator graphical shed spacing after icing, as seen in Table 1, where $D_l{}'$, $D_r{}'$, and $D_a{}'$ represent the left, right, and average graphical shed spacing after icing, respectively. $\triangle D_l$ (%), $\triangle D_r$ (%), and $\triangle D_a$ (%) represent change percentage of the left, right, and average graphical shed spacing after icing, respectively. The computation of $\triangle D_a$ (%) is shown as Equation (7), $\triangle D_m$ (%) denotes the maximum absolute value of change percentage of graphical shed spacing for an insulator string.

Table 1. The change percentage of insulator graphical shed spacing after icing

Grounp	$D_l{}'$	$\triangle D_l$ (%)	$D_r{}'$	$\triangle D_r$ (%)	$D_a{}'$	$\triangle D_a$ (%)	$\triangle D_m$ (%)
Group 1	80.00	6.65%	79.00	8.20%	77.77	−2.45%	−15.96%
	79.00	−15.96%	73.06	−5.13%			
Group 2	47.01	0.00%	46.53	13.18%	47.14	6.33%	14.82%
	50.00	0.00%	45.01	14.82%			
Group 3	-	-	85.05	1.13%	85.05	1.13%	1.13%
Group 4	69.35	−9.13%	76.06	2.78%	55.10	−15.67%	−35.28%
	69.18	−1.21%	69.00	−3.06%			
	42.19	−35.28%	69.01	−10.39%			
	62.65	7.76%	53.08	3.75%			
	40.01	−16.94%	66.00	6.11%			
	22.36	-	-	-			

From the Table 1, it is evident that the changes of average graphical shed spacing for insulators with ice is small ($|\triangle D_a$ (%)$| < 20\%$). In Group 2, $\triangle D_l$ (%) = 0, which indicates that, in the worst icing conditions, sheds are completely bridged in the radial direction. In Group 3, graphical shed spacing and graphical shed overhang cannot be detected due to visual angle.

The change percentages of graphical shed overhang for insulators with ice are shown in Table 2, where $P_l{}'$, $P_r{}'$, and $P_a{}'$ represent the left, right and average graphical shed overhang after icing, respectively. $\triangle P_l$ (%), $\triangle P_r$ (%), and $\triangle P_a$ (%) represent the change percentage of left, right, and average graphical shed overhang after icing, respectively, and the computation of $\triangle P_a$ (%) is shown in Equation (8), and $\triangle P_m$ (%) denotes the maximum absolute value of change percentage of graphical shed overhang for an insulator string.

Table 2. The change percentage of graphical insulator overhang after icing

Grounp	$P_l{}'$	$\triangle P_l$ (%)	$P_r{}'$	$\triangle P_r$ (%)	$P_a{}'$	$\triangle P_a$ (%)	$\triangle P_m$ (%)
Group 1	27.00	−47.06%	28.00	−48.15%	26.75	−49.77%	−66.67%
	34.00	−37.04%	18.00	−66.67%			
Group 2	0.00	−100.00%	16.00	−40.74%	8.00	−68.32%	−100%
	0.00	−100.00%	16.00	−33.33%			
Group 3	-	-	20.00	−20.00%	20.00	−20.00%	−20.00%
Group 4	25.00	−41.86%	47.00	4.44%	22.64	−16.47%	−52.5%
	23.00	−14.81%	19.00	−52.50%			
	20.00	−9.09%	25.00	−19.35%			
	24.00	14.29%	15.00	−11.76%			
	25.00	92.31%	14.00	16.67%			
	12.00	-	-	-			

$|\triangle P_a$ (%)$|$ is much larger than $|\triangle D_a$ (%)$|$ in heavy ice. For example, $\triangle D_a$ (%) in Group 1, Group 2 and Group 3 are −2.45%, 6.33%, and 1.13%, respectively. However, $\triangle P_a$ (%) of these are −49.77%, −68.32%, and −20%, respectively. In Group 2, graphical shed spacing is completely bridged after icing, where $\triangle P_l$ (%) = −100%. When the number of insulator sheds is much larger, the bridging degree in different positions and directions may differ. It is significant to concern the worst icing

conditions. For example, in Group 4, $\triangle P_a$ (%) is -16.47%, while $\triangle P_m$ (%) is -52.5%. However, in Group 4, icing on the bottom three insulator sheds is quite irregular, estimation via change percent of graphical shed overhang after icing has errors.

4. Conclusions

In this paper, graphical shed spacing and graphical shed overhang of in-service glass insulators are proposed to assess insulator icing conditions. This is implemented with GrabCut segmentation and contour convexity defect recognition. The main conclusions are as follows.

The GrabCut segmentation algorithm is proposed to process images of the ice-covered insulator. Compared with the other four image processing methods, the GrabCut algorithm is more superior to extract the contours of the ice-covered insulator from original images. Based on GrabCut segmentation algorithm, graphical shed overhang and graphical shed spacing are calculated using contour convexity defect recognition. The overall icing condition for an insulator string is calculated by average and maximum graphical shed spacing and graphical shed overhang. The results show that the graphical shed overhang of insulators show evident change due to icing. This method can recognize icing conditions quantitatively, e.g., the heavy ice from radial insulator sheds are completely bridged where $\triangle P_l$ (%) = -100%. Also, it can detect bridging position including the left side, the right side, or both sides of the insulator strings in the image.

Author Contributions: Y.H., L.Y. and X.J. conceived and designed the experiments; J.W. performed the experiments; Y.H., J.W., L.Y. and X.J. analyzed the data; J.W., H.L., and R.L. contributed reagents/materials/ analysis tools; J.W., Y.H., and X.J. wrote the paper.

Conflicts of Interest: The authors declare no conflict of interest.

References

1. Liao, R.; Zuo, Z.; Guo, C.; Zhuang, A.; Yuan, Y.; Zhao, X.; Zhang, Y. Ice accretion on superhydrophobic insulators under freezing condition. *Cold Reg. Sci. Technol.* **2015**, *112*, 87–94. [CrossRef]
2. Farzaneh, M. Insulator icing flashover. In Proceedings of the 2013 IEEE Conference on Electrical Insulation and Dielectric Phenomena (CEIDP), Ottata, ON, Canada, 20–23 October 2013; pp. 1–15.
3. Jiang, X.; Xiang, Z.; Zhang, Z.; Hu, J.; Hu, Q.; Shu, L. Comparison on ac icing flashover performance of porcelain, glass, and composite insulators. *Cold Reg. Sci. Technol.* **2014**, *100*, 1–7. [CrossRef]
4. Hu, Q.; Wang, S.; Yang, H.; Shu, L.; Jiang, X.; Li, H.; Qi, J.; Liu, Y. Effects of icing degree on ice growth characteristics and flashover performance of 220 kv composite insulators. *Cold Reg. Sci. Technol.* **2016**, *128*, 47–56. [CrossRef]
5. Oikonomou, D.S.; Maris, T.I.; Ekonomou, L. Artificial intelligence assessment of sea salt contamination of medium voltage insulators. In Proceedings of the 8th WSEAS International Conference on Systems Theory and Scientific Computation (ISTASC'08), Rodos Island, Greece, 20–22 August 2008; pp. 319–323.
6. Pappas, S.S.; Ekonomou, L. Comparison of adaptive techniques for the prediction of the equivalent salt deposit density of medium voltage insulators. *WSEAS Trans. Power Syst.* **2017**, *12*, 220–224.
7. Farzaneh, M. Insulator flashover under icing conditions. *IEEE Trans. Dielectr. Electr. Insul.* **2014**, *21*, 1997–2011. [CrossRef]
8. Berlijn, S.M.; Gutman, I.; Halsan, K.A.; Eilertsten, M.; Gu, I.Y. Laboratory Tests and Web Based Surveillance to Determine the Ice- and Snow Performance of Insulators. *IEEE Trans. Dielectr. Electr. Insul.* **2007**, *14*, 1373–1380. [CrossRef]
9. Wang, X.; Hu, J.; Wu, B.; Du, L.; Sun, C. Study on Edge Extraction Methods for Image-based Icing On-line Monitoring on Overhead Transmission Lines. In Proceedings of the International Conference on High Voltage Engineering and Application, Chongqing, China, 9–13 November 2008; pp. 661–665.
10. Huang, X.; Zhang, Y.; Cheng, W.; Li, M.; Luo, B.; Zhou, K. Galloping Monitoring Method of Transmission Line Based on Image Matching. *High Voltage Eng.* **2015**, *41*, 808–813.

11. Hao, Y.; Liu, G.; Xue, Y.; Zhu, J.; Shi, Z.; Li, L.; School of Electric Power; South China University of Technology. Wavelet Image Recognition of Ice Thickness on Transmission Lines. *High Voltage Eng.* **2014**, *40*, 368–373.

12. Li, Z.T.; Hao, Y.P.; Li, L.C.; Yang, L.; Fu, C. Image Recognition of Ice Thickness on Transmission Lines Using Remote System. *High Voltage Eng.* **2011**, *31*, 76–80.

13. Wang, J.; Wang, J.; Shao, J.; Li, J. Image Recognition of Icing Thickness on Power Transmission Lines Based on a Least Squares Hough Transform. *Energies.* **2017**, *10*, 415. [CrossRef]

14. Wu, Q.; An, J. An active contour model based on texture distribution for extracting inhomogeneous insulators from aerial images. *IEEE Trans. Geosci. Remote Sens.* **2014**, *52*, 3613–3626. [CrossRef]

15. Wu, Q.; An, J.; Lin, B. A texture segmentation algorithm based on PCA and global minimization active contour model for aerial insulator images. *IEEE J. Sel. Top. Appl. Earth Obs. Remote Sens.* **2012**, *5*, 1509–1518.

16. Li, B.; Wu, D.; Cong, Y.; Xia, Y.; Tang, Y. A method of insulator detection from video sequence. In Proceedings of the 2012 International Symposium on Information Science and Engineering (ISISE), Shanghai, China, 14–16 December 2012; pp. 386–389.

17. Zhao, Z.; Jin, S.; Liu, Y. Aerial insulator image edge extraction method based on NSCT. *Chin. J. Sci. Instrum.* **2012**, *33*, 2045–2052.

18. Yang, L.; Jiang, X.; Hao, Y.; Li, L.; Li, H.; Li, R.; Luo, B. Recognition of Natural Ice Types on In-service Glass Insulators Based on Texture Feature Descriptor. *IEEE Trans. Dielectr. Electr. Insul.* **2017**, *24*, 535–542. [CrossRef]

19. Ling, F.; Huang, X.; Zhu, Y. Transmission line icing thickness measuring based on image processing. *Electr. Power Autom. Equip.* **2011**, *31*, 76–80.

20. Yang, H.; Wu, W. On-line Monitoring Method of Icing Transmission Lines Based on 3D reconstruction. *Autom. Electr. Power Syst.* **2012**, *36*, 103–108.

21. Yang, H.; Wu, W. Insulator icing monitoring based on 3D image reconstruction. *Electr. Power Autom. Equip.* **2013**, *32*, 92–98.

22. Yuan, J.; Bae, E.; Tai, X. A spatially continuous max-flow and min-cut framework for binary labeling problems. *Numerische Math.* **2014**, *126*, 559–587. [CrossRef]

23. Melnykov, V.; Melnykov, I. On K-means algorithm with the use of Mahalanobis distances. *Stat. Probab. Lett.* **2014**, *84*, 88–95. [CrossRef]

24. Rockafellar, R.T. *Convex Analysis*; Princeton University Press: Princeton, NJ, USA, 2015.

25. Wang, Y. A new image threshold segmentation based on fuzzy entropy and improved intelligent optimization algorithm. *J. Multimedia* **2014**, *9*, 499–505. [CrossRef]

26. Melin, P.; Gonzalez, C.I.; Castro, J.R.; Mendoza, O.; Castillo, O. Edge-detection method for image processing based on generalized type-2 fuzzy logic. *IEEE Trans. Fuzzy Syst.* **2014**, *22*, 1515–1525. [CrossRef]

27. Görgel, P.; Sertbas, A.; Ucan, O.N. Mammographical mass detection and classification using local seed region growing–spherical wavelet transform (LSRG–SWT) hybrid scheme. *Comput. Biol. Med.* **2013**, *43*, 765–774. [CrossRef] [PubMed]